Acoustic streaming induced by two orthogonal ultrasound standing waves in a microfluidic channel

Alexander A. Doinikov *, Pierre Thibault, Philippe Marmottant

LIPhy UMR 5588, CNRS/Université Grenoble-Alpes, Grenoble F-38401, France

ARTICLE INFO

ABSTRACT

A mathematical model is derived for acoustic streaming in a microfluidic channel confined between a solid wall and a rigid reflector. Acoustic streaming is produced by two orthogonal ultrasound standing waves of the same frequency that are created by two pairs of counter-propagating leaky surface waves induced in the solid wall. The magnitudes and phases of the standing waves are assumed to be different. Full analytical solutions are found for the equations of acoustic streaming. The obtained solutions are used in numerical simulations to reveal the structure of the acoustic streaming. It is shown that the inter-action of two standing waves leads to the appearance of a cross term in the equations of acoustic stream-ing. If the phase lag between the standing waves is nonzero, the cross term brings about circular vortices with rotation axes perpendicular to the solid wall of the channel. The vortices make fluid particles rotate and move alternately up and down between the solid wall and the reflector. The obtained results are of immediate interest for acoustomicrofluidic applications such as the ultrasonic micromixing of fluids and the manipulation of microparticles.

© 2018 Elsevier B.V. All rights reserved.

1. Introduction

The operation of microfluidic systems is based on the use of physical effects produced by ultrasound waves in a microscale environment. Characteristic dimensions of microfluidic devices lie in the range of several micrometers to several hundred micrometers. The sizes of objects whose behavior and properties are investigated in microfluidics are from several nanometers to several micrometers. These conditions require the application of acoustic wave fields with frequencies from the upper kHz range up to several tens of MHz, so processes that occur in microfluidic devices are of ultrasonic nature.

The present work studies theoretically acoustic streaming in an ultrasonically actuated microfluidic channel. Acoustic streaming, along with acoustic radiation forces [1], is one of the main tools that are used in microscale acoustofluidics for contactless manipulation of various objects, such as functionalized microparticles and biological cells [2–4]. Another challenging problem of microfluidics, where acoustic streaming plays a key role, is ultrasonic micromixing of liquid solutions in microfluidic devices. The use of acoustic streaming allows one to enhance this process [5–7]. A detailed special-purpose review on applications of acoustic streaming in microfluidic systems has been provided by Wiklund et al. [8].

In acoustofluidic devices, acoustic streaming is generally boundary layer driven streaming, which is caused by boundary layer effects between an acoustically excited fluid and solid boundaries [8]. A first mathematical description of boundary layer driven streaming was given by Rayleigh [9]. Based on a number of assumptions, he derived a solution for the case of a plane standing wave propagating between two planar rigid walls. His solution predicts acoustic streaming outside the viscous boundary layer and is commonly referred to as "Rayleigh streaming" or "outer streaming". Further development of Rayleigh's theory has been performed by Schlichting [10], Westervelt [11], and Nyborg [12–14]. These studies are reviewed by Boluriaan and Morris [15] and Wiklund et al. [8]. Hamilton et al. [16] have obtained an analytical solution for acoustic streaming generated by a standing wave between two planar rigid walls that allows one to calculate the streaming field both outside and inside the boundary viscous layer. Recently, Doinikov et al. [17] have generalized the solution of Hamilton et al. [16] to the case of two orthogonal standing waves of the same frequency and shown that the interaction between the waves generates acoustic streaming that makes the fluid rotate in planes parallel to the walls. There are also a number of numerical simulations of boundary layer driven streaming, which are reviewed by Boluriaan and Morris [15], see also [18,19].

---

* Corresponding author.
  E-mail address: alexander.doinikov@univ-grenoble-alpes.fr (A.A. Doinikov).

The theoretical studies described above assume that the boundaries, in which an ultrasonically activated fluid is confined, are fixed. In other words, they assume that it is not the vibrational motion of the boundaries that drives the fluid. However, in acoustofluidic devices, the fluid is commonly excited through the vibration of microchannel walls. Muller et al. [18] and Lei et al. [19,20] performed numerical simulations of boundary layer driven acoustic streaming in bulk acoustic wave (BAW) based systems; see also [21] for additional theoretical and experimental data. BAW-based systems are actuated by a piezo transducer attached to the wall of a liquid-filled microchannel. As a result, an acoustic wave is generated in the fluid, which propagates perpendicularly to the vibrating wall. Lei et al. [19,20] showed that, in addition to the classical boundary-driven acoustic streaming, such as Rayleigh streaming whose vortex plane is perpendicular to the transducer face, streaming flows can arise in a plane parallel to the transducer face. Such streaming patterns, named transducer-plane streaming, are typically generated in planar microfluidic resonators, where the acoustic energy gradients in the lateral directions parallel to the transducer face are significant in addition to the gradients perpendicular to the transducer face. The existence of this kind of acoustic streaming is confirmed experimentally [8,19,22].

In recent years, surface acoustic wave (SAW) based systems have gained wide application in microfluidics [23–26]. SAW-based systems are actuated by leaky surface waves that are excited in a solid substrate. These waves propagate along the solid-fluid interface of a microfluidic channel and emit acoustic energy into the fluid layer. As a result, acoustic waves, and hence acoustic streaming, are generated in the fluid. In the context of our theoretical study, relevant works to be mentioned are as follows. Vanneste and Bühler [27] have calculated acoustic streaming produced by a leaky surface wave in a fluid layer with a free boundary. Based on a number of assumptions, they derived linear analytical solutions and then solved numerically the equations of acoustic streaming. Nama et al. [28] applied a finite element scheme to model numerically the acoustophoretic motion of particles inside a liquid-filled PDMS microchannel due to acoustic radiation forces and acoustic streaming. They used impedance boundary conditions to model the channel walls and assumed that the system was actuated by two counter-propagating surface acoustic waves that formed a standing wave in a piezoelectric material interfacing the liquid channel. Their results showed that excited acoustic fields were significantly different from those observed in BAW-based systems. Recently, Doinikov et al. [29] have derived analytical solutions for acoustic streaming in a microfluidic channel confined between an elastic solid wall and a rigid reflector, assuming that the acoustic streaming is generated by a standing wave that is created by two counter-propagating leaky surface waves induced in the solid wall. A discussion of rotational motion that can be induced by acoustic streaming in SAW-driven systems is provided by Bernard et al. [30].

The aim of our study is to develop a theory that describes acoustic streaming in a microfluidic channel confined between an elastic solid wall and a rigid reflector. We assume that the ultrasonic actuation of the above system is produced by two orthogonal ultrasound standing waves of the same frequency that are created by two pairs of counter-propagating leaky surface waves induced in the solid wall. It should be emphasized that the standing waves are assumed to have, in general, different magnitudes and phases. In Section 2, analytical solutions to the equations of acoustic streaming are derived. In Section 3, numerical examples are provided that demonstrate the structure of the acoustic streaming under study. To anticipate, we show that, if the phase lag between the driving standing waves is nonzero, the acoustic streaming produces circular vortices in which fluid particles rotate about axes

perpendicular to the solid wall of the channel and move alternately up and down between the solid wall and the reflector.

2. Theoretical model

2.1. Problem formulation

Let us consider a fluid layer that is confined between an elastic solid wall and a rigid reflector, as shown in Fig. 1. The solid wall occupies the half-space with $z > 0$, the fluid is within the spatial layer with $-h < z < 0$, and the reflector is located at $z = -h$. We assume that two pairs of counter-propagating leaky surface waves are excited in the solid wall. The waves are emitted in the fluid, reflected at the channel top and produce two orthogonal ultrasound standing waves in the channel, which propagate along the x and y axes. The standing waves are assumed to have the same frequency but, in general, different magnitudes and phases.

2.2. Linear solutions

The linear fluid velocity can be represented as

$$\boldsymbol{v} = \boldsymbol{v}_x(x, z, t) + \boldsymbol{v}_y(y, z, t), \tag{1}$$

where

$$\boldsymbol{v}_x = [v_{xx}(x, z)\boldsymbol{e}_x + v_{xz}(x, z)\boldsymbol{e}_z]e^{-i\omega t}, \tag{2}$$

is the velocity produced by the standing wave propagating along the x axis and

$$\boldsymbol{v}_y = [v_{yy}(y, z)\boldsymbol{e}_y + v_{yz}(y, z)\boldsymbol{e}_z]e^{-i\omega t}, \tag{3}$$

is the velocity produced by the standing wave propagating along the y axis. The expression for $\boldsymbol{v}_x$ was derived in our previous paper [29]. An expression for $\boldsymbol{v}_y$ can be written by analogy, just replacing x with y. As a result, expressions for the velocity components can be represented as

$$v_{\tau\tau}(\tau, z) = 2i[iks_{1\tau}(z) - q_v s_{2\tau}(z)]\sin(k\tau), \tag{4}$$

$$v_{\tau z}(\tau, z) = 2[q_f s_{3\tau}(z) + iks_{4\tau}(z)]\cos(k\tau). \tag{5}$$

Here, τ denotes x or y and the following definitions are used:

$$s_{1\tau}(z) = A_{1\tau}e^{q_f z} + A_{2\tau}e^{-q_f z}, \tag{6}$$
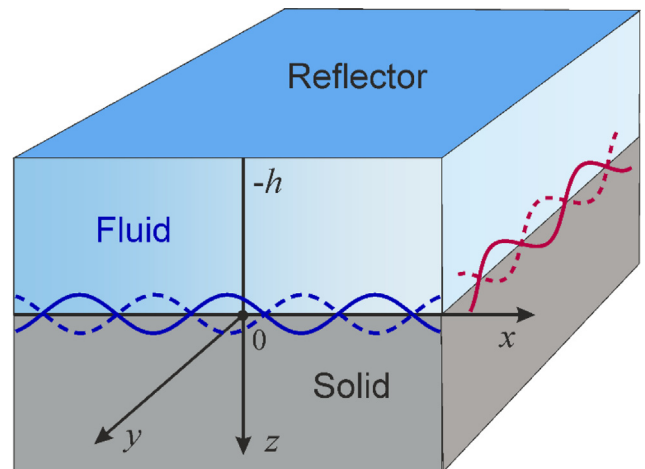
Fig. 1. A fluid layer of height h is located between an elastic solid wall and a rigid reflector. Two orthogonal surface acoustic waves are excited in the solid wall. The waves are emitted in the fluid, reflected at the channel top and produce two orthogonal ultrasound standing waves in the channel, which propagate along the x and y axes.

$$s_{2\tau}(z) = B_{1\tau}e^{q_\nu z} - B_{2\tau}e^{-q_\nu z}, \tag{7}$$

$$s_{3\tau}(z) = A_{1\tau}e^{q_f z} - A_{2\tau}e^{-q_f z}, \tag{8}$$

$$s_{4\tau}(z) = B_{1\tau}e^{q_\nu z} + B_{2\tau}e^{-q_\nu z}, \tag{9}$$

$$q_f = \sqrt{k^2 - k_f^2}, \quad q_\nu = \sqrt{k^2 - k_\nu^2}, \tag{10}$$

$$k_f = \frac{\omega}{c_f}\left[1 - \frac{i\omega}{\rho_f c_f^2}\left(\xi + \frac{4}{3}\eta\right)\right]^{-1/2}, \tag{11}$$

$$k_\nu = \frac{1+i}{\delta_\nu}, \quad \delta_\nu = \sqrt{\frac{2\nu}{\omega}}, \quad \nu = \frac{\eta}{\rho_f}, \tag{12}$$

k is the wavenumber of the leaky surface waves, given by (44) (or (57)) in [29] (note that k is a complex number and hence includes attenuation), c_f is the speed of sound in the fluid, ρ_f is the fluid density at rest, η is the shear viscosity, ξ is the bulk viscosity, δ_ν is the viscous penetration depth and ν is the kinematic viscosity. To obtain the components of the x wave, one should set $\tau = x$ in the above equations, and for the y wave, $\tau = y$. $A_{1\tau}$, $A_{2\tau}$, $B_{1\tau}$, and $B_{2\tau}$ are complex constants that describe the magnitudes and the phases of the standing waves. It is shown in [29] that these constants are expressed in terms of the complex amplitudes of the driving surface waves, which are activated in the solid wall. Thus, setting the magnitudes and the phases of the driving x and y surface waves, one can set relative magnitudes and phases of the induced x and y standing waves, which produce acoustic streaming in the fluid.

For detailed information on the linear solutions, the reader is referred to our previous paper [29], where these solutions are derived.

2.3. Acoustic streaming

2.3.1. Equations of acoustic streaming

Let us denote the Eulerian mean velocity by $\boldsymbol{V}$. We will follow the approximation proposed by Nyborg [13], which assumes that the Eulerian mean velocity behaves as a velocity of an incompressible flow so that one can write

$$\nabla \cdot \boldsymbol{V} = 0. \tag{13}$$

This approximation makes the problem amenable to analytical consideration. Arguments in support of this approximation are that compressibility effects usually play an important role at large Mach numbers or when wave propagation over large distances is considered. Both these situations are not characteristic of acoustic streaming.

From [13], it also follows that in the second-order approximation with respect to the linear solutions, $\boldsymbol{V}$ obeys the following equation:

$$\nu\Delta\boldsymbol{V} - \frac{1}{\rho_f}\nabla P = \langle(\boldsymbol{v}\cdot\nabla)\boldsymbol{v} + \boldsymbol{v}(\nabla\cdot\boldsymbol{v})\rangle, \tag{14}$$

where P is the time averaged second-order pressure and $\langle\rangle$ means time averaging.

Eq. (13) is satisfied if we set

$$\boldsymbol{V} = \nabla \times \boldsymbol{\Psi}. \tag{15}$$

Substituting (15) into (14) and applying the curl operator, one obtains

$$\Delta^2\boldsymbol{\Psi} = -\frac{1}{\nu}\nabla \times \boldsymbol{W}, \tag{16}$$

where with accuracy up to leading terms $\boldsymbol{W}$ is given by [29]

$$\boldsymbol{W} = \langle(\boldsymbol{v}_x\cdot\nabla + \boldsymbol{v}_y\cdot\nabla)(\boldsymbol{v}_x + \boldsymbol{v}_y)\rangle. \tag{17}$$

Eq. (17) shows that $\boldsymbol{W}$ can be represented as

$$\boldsymbol{W} = \boldsymbol{W}_x(x,z) + \boldsymbol{W}_y(y,z) + \boldsymbol{U}(x,y,z), \tag{18}$$

where

$$\boldsymbol{W}_x(x,z) = \langle(\boldsymbol{v}_x\cdot\nabla)\boldsymbol{v}_x\rangle, \boldsymbol{W}_y(y,z) = \langle(\boldsymbol{v}_y\cdot\nabla)\boldsymbol{v}_y\rangle, \tag{19}$$

and

$$\boldsymbol{U}(x,y,z) = \langle(\boldsymbol{v}_x\cdot\nabla)\boldsymbol{v}_y + (\boldsymbol{v}_y\cdot\nabla)\boldsymbol{v}_x\rangle. \tag{20}$$

The terms $\boldsymbol{W}_x$ and $\boldsymbol{W}_y$ describe the acoustic streaming produced by the x and y waves, respectively, as if the second wave were absent. The expression for the streaming velocity $\boldsymbol{V}_x$ that is produced by $\boldsymbol{W}_x$ was derived in our paper [29]. An expression for the streaming velocity $\boldsymbol{V}_y$ produced by $\boldsymbol{W}_y$ can be written by analogy, replacing x with y in the expression for $\boldsymbol{V}_x$. Therefore, we can consider these two contributions as known.

Eq. (20) gives a cross term that arises because the right-hand side of (14) includes products that are dependent on both x and y simultaneously. The aim of the calculation that follows is to derive a streaming velocity that is produced by the cross term. Let us denote this velocity by $\boldsymbol{V}^\otimes$. It can be represented as

$$\boldsymbol{V}^\otimes = \nabla \times \boldsymbol{\Psi}^\otimes, \tag{21}$$

where $\boldsymbol{\Psi}^\otimes$ denotes the vector potential. We will see in Section 3 that it is the contribution of $\boldsymbol{V}^\otimes$ that gives rise to fluid rotation in the xy planes.

2.3.2. Calculation of $\boldsymbol{V}^\otimes$

Since $\boldsymbol{v}_x$ does not depend on y and $\boldsymbol{v}_y$ does not depend on x, the components of $\boldsymbol{U}$ along the coordinate axes are written as follows:

$$U_x = \frac{1}{2}\text{Re}\left\{v_{yz}^*\frac{\partial v_{xx}}{\partial z}\right\}, \tag{22}$$

$$U_y = \frac{1}{2}\text{Re}\left\{v_{xz}\frac{\partial v_{yy}^*}{\partial z}\right\}, \tag{23}$$

$$U_z = \frac{1}{2}\text{Re}\left\{\frac{\partial}{\partial z}\left(v_{xz}v_{yz}^*\right)\right\}, \tag{24}$$

where the asterisk denotes the complex conjugate. We have used (2) and (3) here.

Let us represent $\boldsymbol{\Psi}^\otimes$ as

$$\boldsymbol{\Psi}^\otimes = \Psi_1\boldsymbol{e}_x + \Psi_2\boldsymbol{e}_y + \Psi_3\boldsymbol{e}_z. \tag{25}$$

Then it follows from (16) that

$$\Delta^2\Psi_1 = \frac{1}{\nu}\left(\frac{\partial U_y}{\partial z} - \frac{\partial U_z}{\partial y}\right), \tag{26}$$

$$\Delta^2\Psi_2 = \frac{1}{\nu}\left(\frac{\partial U_z}{\partial x} - \frac{\partial U_x}{\partial z}\right), \tag{27}$$

$$\Delta^2\Psi_3 = \frac{1}{\nu}\left(\frac{\partial U_x}{\partial y} - \frac{\partial U_y}{\partial x}\right). \tag{28}$$

Substituting (4) and (5) into (22)–(24), then substituting the results into (26)–(28) and using the fact that $k_\nu^{2*} = -k_\nu^2$, one obtains

$$\Delta^2\Psi_1 = \frac{1}{\nu}\text{Re}\left\{ik_\nu^2 F_1(z)[\sin(kx + k^*y) - \sin(kx - k^*y)]\right\}, \tag{29}$$

$$\Delta^2\Psi_2 = \frac{1}{\nu}\text{Re}\left\{ik_\nu^2 F_2(z)[\sin(kx + k^*y) + \sin(kx - k^*y)]\right\}, \tag{30}$$

$$\Delta^2\Psi_3 = \frac{1}{v}\text{Re}\Big\{ik_v^2F_3(z)[\cos(kx+k^*y)-\cos(kx-k^*y)]\Big\}, \quad (31)$$

where the functions $F_n(z)$ are calculated by

$$F_1(z) = q_f^2 s_{1x}s_{4y}^* + q_f q_v^* s_{3x}s_{2y}^* + ikq_v s_{2x}s_{4y}^* + ikq_v^* s_{4x}s_{2y}^*, \quad (32)$$

$$F_2(z) = ik^* q_v s_{2x}s_{4y}^* + ik^* q_v^* s_{4x}s_{2y}^* - q_f^2 q_v s_{2x}s_{3y}^* - q_f^{2*} s_{4x}s_{1y}^*, \quad (33)$$

$$F_3(z) = k^* q_f^* s_{4x}s_{3y}^* - kq_f s_{3x}s_{4y}^* - i(k^2+k^{2*})s_{4x}s_{4y}^*. \quad (34)$$

When deriving these equations, we have used the following identities:

$$s_{1\tau}' = q_f s_{3\tau}, \quad s_{2\tau}' = q_v s_{4\tau}, \quad s_{3\tau}' = q_f s_{1\tau}, \quad s_{4\tau}' = q_v s_{2\tau}, \quad (35)$$

which follow from (6)–(9), the prime denoting the derivative with respect to z.

Solutions to (29)–(31) can be sought in the following from:

$$\Psi_1 = \frac{1}{v}\text{Re}\Big\{ik_v^2 G_1(z)[\sin(kx+k^*y)-\sin(kx-k^*y)]\Big\}, \quad (36)$$

$$\Psi_2 = \frac{1}{v}\text{Re}\Big\{ik_v^2 G_2(z)[\sin(kx+k^*y)+\sin(kx-k^*y)]\Big\}, \quad (37)$$

$$\Psi_3 = \frac{1}{v}\text{Re}\Big\{ik_v^2 G_3(z)[\cos(kx+k^*y)-\cos(kx-k^*y)]\Big\}, \quad (38)$$

where $G_n(z)$ are sought-for functions. Substitution of (36)–(38) into (29)–(31) yields

$$\frac{d^4 G_n}{dz^4} - 2\alpha^2 \frac{d^2 G_n}{dz^2} + \alpha^4 G_n = F_n(z), \quad (39)$$

where $\alpha = \sqrt{2\text{Re}\{k^2\}}$ and $n = 1, 2, 3$. Solutions to (39) are given by

$$G_n(z) = \psi_n(z) + (c_{n1}+c_{n2}z)e^{\alpha z} + (c_{n3}+c_{n4}z)e^{-\alpha z}, \quad (40)$$

where $\psi_n(z)$ is the particular solution, which arises from the function $F_n(z)$ on the right-hand side of (39) and the other two terms are the homogeneous solutions, in which c_{nm} are constants to be found.

Let us calculate the particular solution $\psi_1(z)$ to (39) with $n = 1$. The structure of $F_1(z)$ and the properties of the products $s_{nx}s_{my}^*$ (see Appendix A) suggest that $\psi_1(z)$ can be sought in the following form:

$$\psi_1(z) = a_{11}s_{1x}s_{4y}^* + a_{12}s_{3x}s_{2y}^* + a_{13}s_{2x}s_{4y}^* + a_{14}s_{4x}s_{2y}^*, \quad (41)$$

where a_{1m} are constants to be found. The derivatives of the products $s_{nx}s_{my}^*$ necessary for the calculation of $\psi_1(z)$ are given in Appendix A. Using them, substituting (41) into (39), and equating terms at the same products $s_{nx}s_{my}^*$ on the left- and right-hand sides, one obtains

$$a_{11} = \frac{q_f^2[(k_f^2-k_v^2)^2+4q_v^2 q_v^{2*}]}{[(k_f^2-k_v^2)^2-4q_f^2 q_v^{2*}]^2}, \quad (42)$$

$$a_{12} = \frac{q_f q_v^*[(k_f^2-k_v^2)^2+4q_f^2(k^{2*}+k_f^2)]}{[(k_f^2-k_v^2)^2-4q_f^2 q_v^{2*}]^2}, \quad (43)$$

$$a_{13} = \frac{ik}{4q_v q_v^{2*}}, \quad (44)$$

$$a_{14} = \frac{ik}{4q_v^2 q_v^*}. \quad (45)$$

Expressions for $\psi_2(z)$ and $\psi_3(z)$ are calculated by the same method. The result is as follows:

$$\psi_2(z) = a_{21}s_{4x}s_{1y}^* + a_{22}s_{2x}s_{3y}^* + a_{23}s_{4x}s_{2y}^* + a_{24}s_{2x}s_{4y}^*, \quad (46)$$

$$\psi_3(z) = a_{31}s_{1x}s_{2y}^* + a_{32}s_{3x}s_{4y}^* + a_{33}s_{2x}s_{1y}^* + a_{34}s_{4x}s_{3y}^* + a_{35}s_{4x}s_{4y}^*, \quad (47)$$

where

$$a_{21} = -a_{11}^*, \quad a_{22} = -a_{12}^*, \quad a_{23} = -a_{13}^*, \quad a_{24} = -a_{14}^*, \quad (48)$$

$$a_{31} = -\frac{4kq_f^2 q_v^*(k_f^2-k_v^2)}{\big[(k_f^2-k_v^2)^2-4q_f^2 q_v^{2*}\big]^2}, \quad (49)$$

$$a_{32} = -\frac{kq_f[(k_f^2-k_v^2)^2+4q_f^2 q_v^{2*}]}{\big[(k_f^2-k_v^2)^2-4q_f^2 q_v^{2*}\big]^2}, \quad (50)$$

$$a_{33} = -a_{31}^*, \quad a_{34} = -a_{32}^*, \quad (51)$$

$$a_{35} = -\frac{i(k^2+k^{2*})}{4q_v^2 q_v^{2*}}. \quad (52)$$

That (46)–(52) satisfy (39) at $n = 2, 3$ can be checked by direct substitution, using the derivatives of $s_{nx}s_{my}^*$ given in Appendix A.

The functions $G_n(z)$ contain 12 unknown constants. We can reduce their number using the fact that $\nabla \times (\nabla\Phi) \equiv 0$, where Φ is an arbitrary scalar function. In view of this fact, the velocity field $\boldsymbol{V}^\otimes$ will not change if we replace $\boldsymbol{\Psi}^\otimes$ with $\widetilde{\boldsymbol{\Psi}}^\otimes = \boldsymbol{\Psi}^\otimes - \nabla\Phi$. Let us take Φ in the following form:

$$\Phi = \frac{1}{v}\text{Re}\Big\{\frac{ik_v^2}{\alpha^2}[(\alpha c_{31}-c_{32}+\alpha c_{32}z)e^{\alpha z} - (\alpha c_{33}+c_{34}+\alpha c_{34}z)e^{-\alpha z}]$$
$$\times[\cos(kx+k^*y)-\cos(kx-k^*y)]\Big\}. \quad (53)$$

Substitution of (53) into $\widetilde{\boldsymbol{\Psi}}^\otimes$ gives modified expressions for $G_n(z)$,

$$G_n(z) = \psi_n(z) + (\widetilde{c}_{n1}+\widetilde{c}_{n2}z)e^{\alpha z} + (\widetilde{c}_{n3}+\widetilde{c}_{n4}z)e^{-\alpha z}, \quad n = 1, 2, \quad (54)$$

$$G_3(z) = \psi_3(z), \quad (55)$$

where $\widetilde{c}_{nm}$ are new constants. As one can see, we have eliminated the constants c_{3m}, while the form of G_1 and G_2 has remained the same. Therefore, we can drop the tilde and denote the constants by c_{1m} and c_{2m} as before. Another way of putting it is that (40) remains valid on condition that $c_{3m} = 0$.

Calculation of the components of $\boldsymbol{V}^\otimes$ gives

$$V_x^\otimes = -\frac{1}{v}\text{Re}\Big\{ik_v^2[G_2'(z)+k^*\psi_3(z)][\sin(kx+k^*y)+\sin(kx-k^*y)]\Big\}, \quad (56)$$

$$V_y^\otimes = \frac{1}{v}\text{Re}\Big\{ik_v^2[G_1'(z)+k\psi_3(z)][\sin(kx+k^*y)-\sin(kx-k^*y)]\Big\}, \quad (57)$$

$$V_z^\otimes = \frac{1}{v}\text{Re}\Big\{ik_v^2[kG_2(z)-k^*G_1(z)][\cos(kx+k^*y)+\cos(kx-k^*y)]\Big\}, \quad (58)$$

where the prime denotes the derivative with respect to z. With the help of the equations in Appendix A, $G_{1,2}'$ are calculated as

$$G_n'(z) = \psi_n'(z) + [\alpha c_{n1}+c_{n2}(1+\alpha z)]e^{\alpha z} - [\alpha c_{n3}-c_{n4}(1-\alpha z)]e^{-\alpha z}, \quad n = 1, 2, \quad (59)$$

$$\psi_1^/(z) = (a_{11}q_v^* + a_{12}q_f)s_{1x}s_{2y}^* + (a_{11}q_f + a_{12}q_v^*)s_{3x}s_{4y}^* + (a_{13}q_v^* + a_{14}q_v)s_{2x}s_{2y}^* + (a_{13}q_v + a_{14}q_v^*)s_{4x}s_{4y}^*, \tag{60}$$

$$\psi_2^/(z) = (a_{21}q_v + a_{22}q_f^*)s_{2x}s_{1y}^* + (a_{21}q_f^* + a_{22}q_v)s_{4x}s_{3y}^* + (a_{23}q_v + a_{24}q_v^*)s_{2x}s_{2y}^* + (a_{23}q_v^* + a_{24}q_v)s_{4x}s_{4y}^*. \tag{61}$$

To find the constants c_{1m} and c_{2m}, we can use no-slip boundary conditions for the streaming velocity at the solid wall and at the reflector. However, these conditions must be applied to the Lagrangian streaming velocity [27,31], which is the velocity of fluid particles specified in the particle coordinates [11]. By definition, the Lagrangian streaming velocity is the sum of the Eulerian streaming velocity $\boldsymbol{V}^\otimes$ and the Stokes drift velocity [27,31,32]. Therefore, we have first to calculate the Stokes drift velocity.

2.3.3. Stokes drift velocity

The full Stokes drift velocity is calculated by [11,32]

$$\boldsymbol{V}_S = \left\langle \int \boldsymbol{v} dt \cdot \nabla \boldsymbol{v} \right\rangle = \frac{1}{\omega}\langle (i\boldsymbol{v} \cdot \nabla)\boldsymbol{v} \rangle. \tag{62}$$

The terms produced by the x wave when the y wave is absent are provided in [29]. The terms produced by the y wave can be calculated by replacing x with y in the x terms. The cross terms, which we will use along with $\boldsymbol{V}^\otimes$, are given by

$$V_{Sx}^\otimes = -\frac{1}{2\omega}\text{Re}\left\{ iv_{yz}^* \frac{\partial v_{xx}}{\partial z} \right\}, \tag{63}$$

$$V_{Sy}^\otimes = \frac{1}{2\omega}\text{Re}\left\{ iv_{xz} \frac{\partial v_{yy}^*}{\partial z} \right\}, \tag{64}$$

$$V_{Sz}^\otimes = \frac{1}{2\omega}\text{Re}\left\{ iv_{xz} \frac{\partial v_{yz}^*}{\partial z} - iv_{yz}^* \frac{\partial v_{xz}}{\partial z} \right\}, \tag{65}$$

Substitution of (4) and (5) yields

$$V_{Sx}^\otimes = \frac{1}{\omega}\text{Re}\{H_1(z)[\sin(kx + k^*y) + \sin(kx - k^*y)]\}, \tag{66}$$

$$V_{Sy}^\otimes = -\frac{1}{\omega}\text{Re}\{H_2(z)[\sin(kx + k^*y) - \sin(kx - k^*y)]\}, \tag{67}$$

$$V_{Sz}^\otimes = \frac{1}{\omega}\text{Re}\{H_3(z)[\cos(kx + k^*y) + \cos(kx - k^*y)]\}, \tag{68}$$

where

$$H_1(z) = (ikq_f s_{3x} - q_v^2 s_{4x})(q_f s_{3y} + iks_{4y})^*, \tag{69}$$

$$H_2(z) = (q_f s_{3x} + iks_{4x})(q_v^2 s_{4y} - ikq_f s_{3y})^*, \tag{70}$$

$$H_3(z) = (kq_v s_{2x} - iq_f^2 s_{1x})(q_f s_{3y} + iks_{4y})^* + (iq_f s_{3x} - ks_{4x})(q_f^2 s_{1y} + ikq_v s_{2y})^*. \tag{71}$$

2.3.4. Calculation of c_{nm}

In order to find the unknown constants c_{1m} and c_{2m} appearing in (40), we use the boundary conditions at the solid wall and at the reflector. These conditions require that the Lagrangian streaming velocity $\boldsymbol{V}_L^\otimes = \boldsymbol{V}^\otimes + \boldsymbol{V}_S^\otimes$ be equal to zero at $z = 0$ and $z = -h$ [27,31]. As a result, we obtain the following equations:

$$G_2^/(z) = \frac{v}{ik_v^2\omega}H_1(z) - k^*\psi_3(z) \text{ at } z = 0, -h, \tag{72}$$

$$G_1^/(z) = \frac{v}{ik_v^2\omega}H_2(z) - k\psi_3(z) \text{ at } z = 0, -h, \tag{73}$$

$$k^*G_1(z) - kG_2(z) = \frac{v}{ik_v^2\omega}H_3(z) \text{ at } z = 0, -h. \tag{74}$$

Eq. (72) contains only c_{2m}, (73) contains only c_{1m}, while (74) contains both c_{1m} and c_{2m}. We can separate c_{1m} and c_{2m} by splitting (74) into two equations, taking into account the symmetry of the problem with respect to x and y. As a result, we obtain two independent systems of equations, one of which is for the unknowns c_{1m},

$$G_1^/(z) = \frac{v}{ik_v^2\omega}H_2(z) - k\psi_3(z) \text{ at } z = 0, -h, \tag{75a}$$

$$G_1(z) = \frac{v}{2ik^*k_v^2\omega}H_3(z) \text{ at } z = 0, -h, \tag{75b}$$

and the other is for the unknowns c_{2m},

$$G_2^/(z) = \frac{v}{ik_v^2\omega}H_1(z) - k^*\psi_3(z) \text{ at } z = 0, -h, \tag{76a}$$

$$G_2(z) = -\frac{v}{2ikk_v^2\omega}H_3(z) \text{ at } z = 0, -h. \tag{76b}$$

Substitution of (40) and (59) into (75a) and (75b) yields the following system of algebraic equations:

$$\begin{pmatrix} \alpha & 1 & -\alpha & 1 \\ \alpha e^{-\alpha h} & (1-\alpha h)e^{-\alpha h} & -\alpha e^{\alpha h} & (1+\alpha h)e^{\alpha h} \\ 1 & 0 & 1 & 0 \\ e^{-\alpha h} & -he^{-\alpha h} & e^{\alpha h} & -he^{\alpha h} \end{pmatrix} \times \begin{pmatrix} c_{11} \\ c_{12} \\ c_{13} \\ c_{14} \end{pmatrix}$$
$$= \begin{pmatrix} \frac{v}{ik_v^2\omega}H_2(0) - \psi_1^/(0) - k\psi_3(0) \\ \frac{v}{ik_v^2\omega}H_2(-h) - \psi_1^/(-h) - k\psi_3(-h) \\ \frac{v}{2ik^*k_v^2\omega}H_3(0) - \psi_1(0) \\ \frac{v}{2ik^*k_v^2\omega}H_3(-h) - \psi_1(-h) \end{pmatrix}. \tag{77}$$

The unknowns c_{1m} are calculated by

$$c_{1m} = \frac{D_{1m}}{D}, \tag{78}$$

where D is the determinant of the coefficient matrix of (77) and D_{1m} is the determinant of the coefficient matrix in which the mth column is replaced with the column of the free terms.

Substitution of (40) and (59) into (76a) and (76b) shows that the coefficient matrix remains the same as in (77), while the free terms are given by

$$\begin{pmatrix} \frac{v}{ik_v^2\omega}H_1(0) - \psi_2^/(0) - k^*\psi_3(0) \\ \frac{v}{ik_v^2\omega}H_1(-h) - \psi_2^/(-h) - k^*\psi_3(-h) \\ -\frac{v}{2ikk_v^2\omega}H_3(0) - \psi_2(0) \\ -\frac{v}{2ikk_v^2\omega}H_3(-h) - \psi_2(-h) \end{pmatrix}. \tag{79}$$

Therefore, the unknowns c_{2m} are calculated by

$$c_{2m} = \frac{D_{2m}}{D}, \tag{80}$$

where D_{2m} is the determinant of the coefficient matrix of (77) in which the mth column is replaced with the column of the free terms from (79).

Now that all the constants are calculated, our derivation is complete. To sum up, we have calculated the streaming velocity $\boldsymbol{V}_L^\otimes = \boldsymbol{V}^\otimes + \boldsymbol{V}_S^\otimes$, which is induced by the cross term in the equations of acoustic streaming; see the end of Section 2.3.1. It should be remembered that $\boldsymbol{V}_L^\otimes$ is only a part of the total Lagrangian streaming velocity, $\boldsymbol{V}_L$, which is produced by two standing waves in the

channel. In addition to $\boldsymbol{V}_L^\otimes$, $\boldsymbol{V}_L$ includes the Lagrangian streaming velocity produced by the x wave when the y wave is absent, $\boldsymbol{V}_{Lx}$, and the Lagrangian streaming velocity produced by the y wave when the x wave is absent, $\boldsymbol{V}_{Ly}$. In other words, the total acoustic streaming is given by $\boldsymbol{V}_L$, which is calculated by

$$\boldsymbol{V}_L = \boldsymbol{V}_{Lx} + \boldsymbol{V}_{Ly} + \boldsymbol{V}_L^\otimes, \tag{81}$$

where $\boldsymbol{V}_{Lx}$ was calculated in our previous paper [29], $\boldsymbol{V}_{Ly}$ is calculated by replacing x with y in the expression for $\boldsymbol{V}_{Lx}$ and $\boldsymbol{V}_L^\otimes$ was calculated in the present study.

3. Numerical simulations

In order to reveal the structure of the acoustic streaming, numerical examples have been considered. The simulations were made at the following physical parameters: $\rho_f = 1000$ kg/m^3, $c_f = 1500$ m/s, $\eta = 0.001$ Pa s, $\xi = 0.003$ Pa s, $\rho_s = 4640$ kg/m^3, $\lambda = 68$ GPa, $\mu = 68$ GPa and $f = \omega/2\pi = 36$ MHz. Here, ρ_s is the density of the solid wall and λ and μ are the Lamé coefficients. The above parameters were chosen to correspond to typical

parameters of microfluidic devices involving a lithium niobate (LiNbO$_3$) substrate to generate acoustic waves by interdigitated transducers (IDTs) [30]. For these parameters, at the channel height $h = 50$ μm, the dispersion equation in [29] gives the wavenumber of the leaky surface wave $k = 62860 + 5.64i$ m^{-1}, which corresponds to the wave speed $c = \omega/\text{Re}[k] = 3598$ m/s, the wavelength $\lambda_{sw} = 99.96$ μm, and the attenuation coefficient $\alpha_{sw} = \text{Im}[k] = 5.64$ m^{-1}. The viscous penetration depth in the fluid is $\delta_v = 94nm \approx 0.002h$. It should be emphasized that the streaming velocity that is calculated in our numerical examples is the Lagrangian streaming velocity. Doing so, we follow Westervelt [11] who pointed out that the velocity of fluid particles involved in acoustic streaming should be specified in the particle coordinates, i.e., that should be the Lagrangian streaming velocity.

Fig. 2 shows streamline patterns that are obtained by projecting the Lagrangian streaming velocity on xy planes at different values of z. The channel height is $h = 50$ μm. The phase lag between the x and y waves is $\phi = \pi/2$. As one can see, the fluid is rotating about vertical axes (z axes) perpendicular to the channel boundaries. The direction of the rotation changes with varying z. For
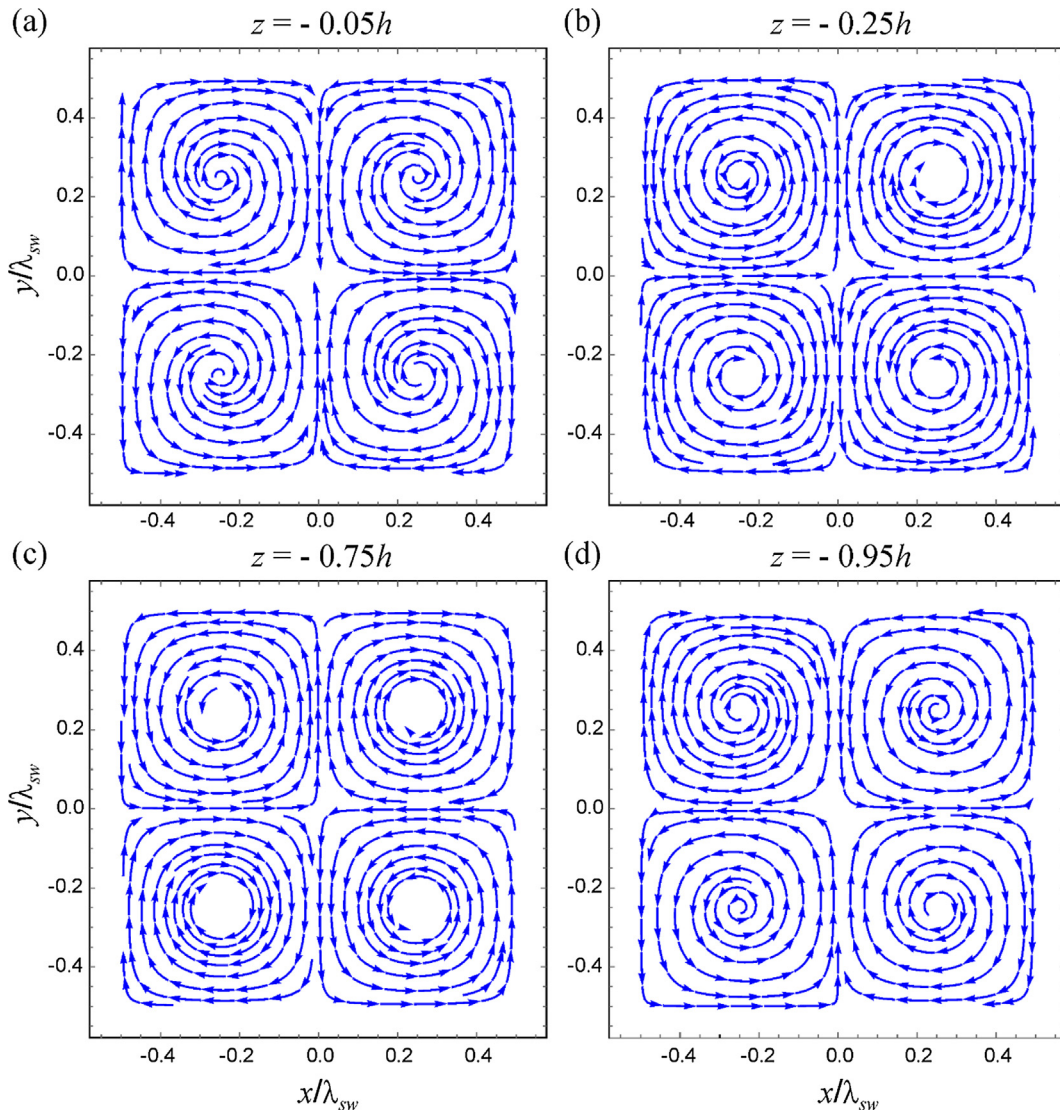
Fig. 2. Projections of streamlines of the Lagrangian streaming velocity on xy planes at different values of z. The channel height h is 50 μm. The phase lag between the x and y waves is $\phi = \pi/2$. The fluid is rotating about the z axes perpendicular to the channel boundaries.

example, if we compare the left top quarter of Fig. 2a with that of Fig. 2b, we see that the rotation changes from clockwise to counterclockwise.

Calculations reveal that rotation arises not only at $\phi = \pi/2$, but in all cases that the phase lag is nonzero. This fact is illustrated by Fig. 3, which shows projections of streamlines on the xy plane at $z = -0.75h$ for different values of ϕ, the other parameters being the same as in Fig. 2.

At $\phi = 0$, the fluid rotation vanishes. This situation is exemplified by Fig. 4, which shows the same case as in Fig. 2 at $\phi = 0$. Calculations also reveal that the rotation is caused by the cross terms of the streaming, i.e., the components of the velocity field $\mathbf{V}^{\otimes}$. As an example, Fig. 5 shows what happens to Fig. 2a and b if the cross terms are eliminated from the calculation. We see that rotation is absent.

The projections of streamlines in Figs. 2 and 3 look like spirals. This form is explained by the fact that fluid particles move over spiral-like trajectories. We will see this below in Figs. 7–9, which give examples of 3D trajectories of fluid particles.

In connection with the fluid rotation described above it is pertinent to mention the following point. There are studies that consider the rotation of a spherical microparticle in the field of two orthogonal standing waves [33,34,30]. They show that, when there is a nonzero phase shift ϕ between the standing waves, an acoustic streaming arises around the particle and produces a nonzero viscous torque on the particle, driving it to rotate around its axis of symmetry. The streaming magnitude is found to be dependent on $\sin\phi$. In our study, a different physical problem is considered. We consider a boundary layer driven streaming, which is caused by boundary layer effects between an acoustically excited fluid and the bounding walls of a microfluidic channel. This streaming gives rise to the rotation of the fluid flow as such. The complicated mathematical form of the streaming solutions does not allow one to see the explicit mathematical form of the dependence on ϕ: if it is $\sin\phi$ or something different. Therefore, it is difficult to conclude if or not there is an analogy with the results reported in [33,34].

Fig. 6 shows projections of streamlines on the xz plane at $y = \lambda_{sw}/4$ for different values of the channel height h. The phase
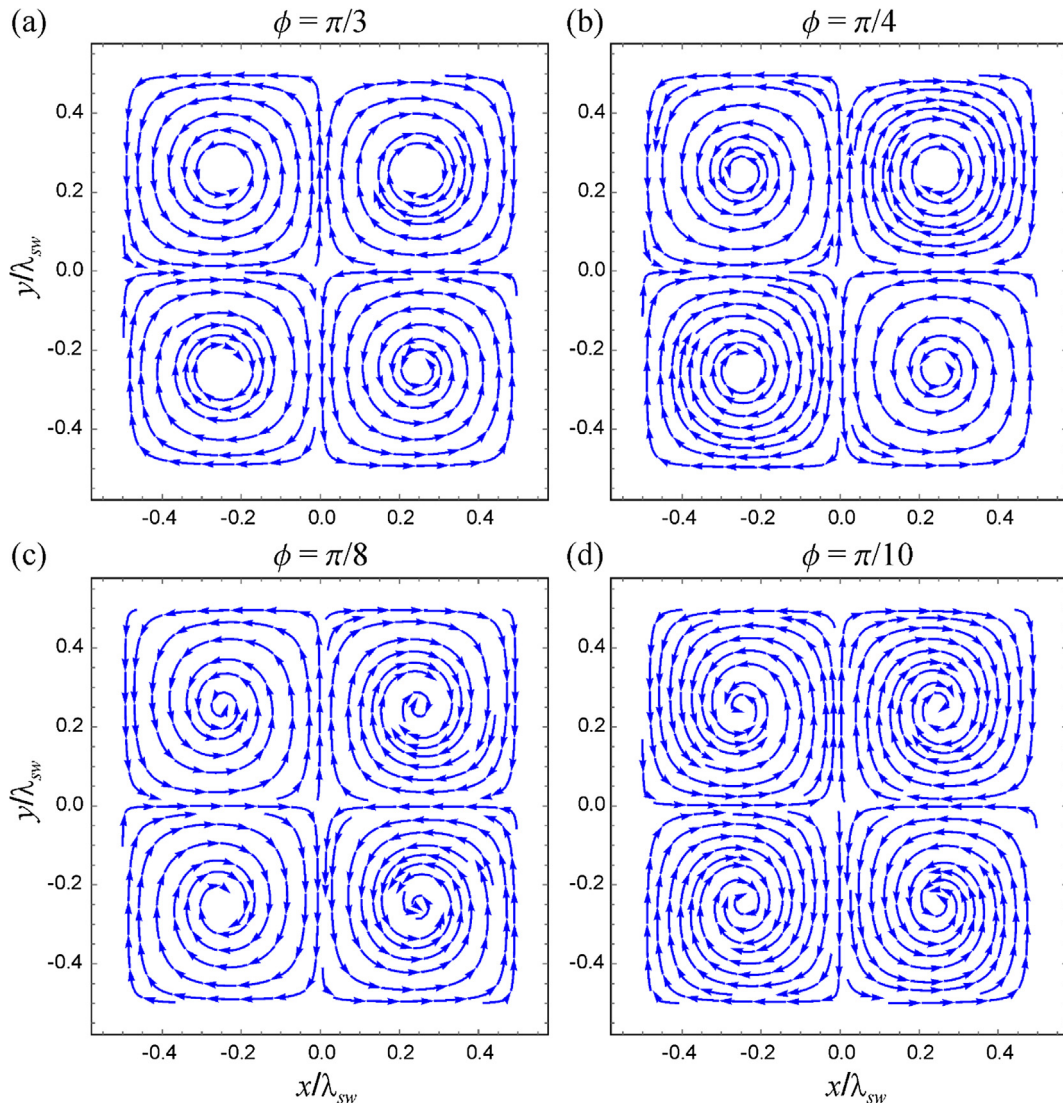
Fig. 3. Projections of streamlines of the Lagrangian streaming velocity on the xy plane at $z = -0.75h$ for different values of the phase lag ϕ. The other parameters are as in Fig. 2. The channel height h is 50 μm. Rotation occurs at all nonzero values of ϕ.

(a)   z = - 0.05h

(b)   z = - 0.25h

(c)   z = - 0.75h

(d)   z = - 0.95h
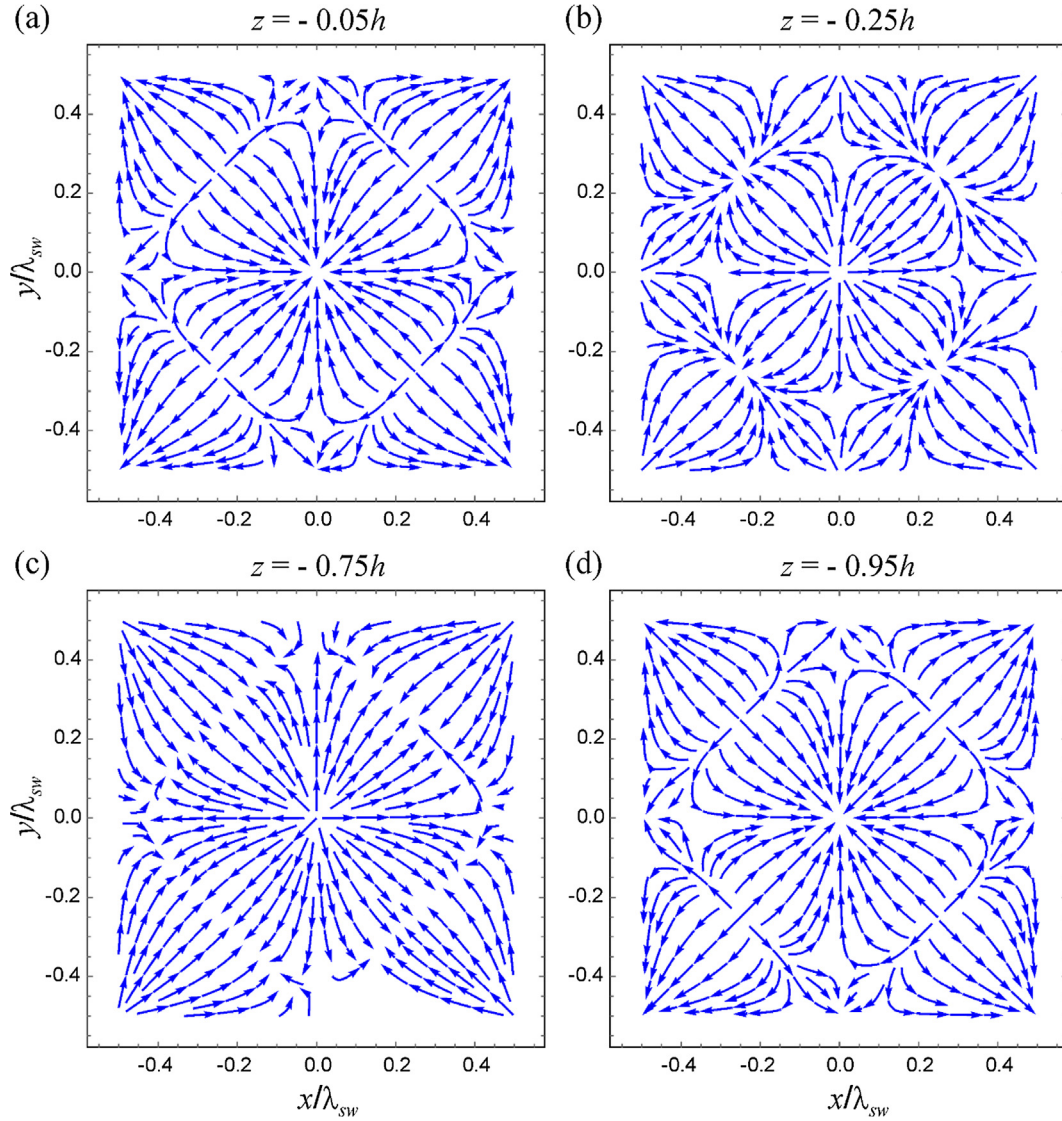
Fig. 4. The same case as in Fig. 2 at the phase lag $\phi = 0$. The channel height h is 50 µm. Rotation vanishes.

lag between the x and y waves is $\phi = \pi/2$. Note that the label 1.0 on the vertical axes corresponds to the position of the reflector. As one can see, the streaming consists of upper and lower parts. The position of the division plane and the form of streamlines change with h but the division into upper and lower parts remains at all h.

Figs. 7–9 are examples of 3D trajectories of fluid particles. The calculations were performed at the channel height $h = 50$ µm. Figs. 7 and 8 exemplify the motion of fluid particles in the upper part of the channel. They show that fluid particles are rotating and moving alternately up and down between the reflector and a horizontal plane that divides the channel at $z \approx -0.6h$. As one can see, when a fluid particle is moving up, its rotation radius first decreases. The ascent of the particle occurs mainly along the axis of the vortex. Then the rotation radius increases, and when the particle reaches the edge of the vortex, its motion turns abruptly down. Fig. 7b explains why the projections of streamlines in Figs. 2 and 3 look like spirals. Figs. 7 and 8 also show that there are relatively simple trajectories, such as that in Fig. 7, and more complicated trajectories, such as that in Fig. 8. The trajectory shown in Fig. 7 becomes closed in one up-down pass, while the trajectory in

Fig. 8 does not become closed even after many up-down passes. We call a trajectory closed if, after a certain number of time steps, the numerical simulation shows that the fluid particle comes to the initial point and then moves along the same path. The calculation of trajectories is sensitive to small deviations in space. If the accuracy of the calculation is not sufficient (too large time step), the observed fluid particle can "jump" to another trajectory in the process of the calculation. Therefore, the calculation of trajectories requires a particular accuracy and is time-consuming. Animations of the trajectory shown in Fig. 7 and a part of the trajectory shown in Fig. 8 are provided as supplementary material.

Fig. 9 is an example of the fluid particle trajectory in the lower part of the channel. Just as in the upper part, the fluid particle is rotating and moving up and down. The difference is that the upward motion occurs at the edge of the vortex and the downward motion is executed along the axis of the vortex. The trajectory shown in Fig. 9 is not closed.

Our theory allows one to consider the case that the driving standing waves are of different magnitudes. This case is illustrated by Figs. 10–12. Fig. 10 shows how the xy streamline pattern depicted in Fig. 2a is transformed with varying ε, where ε denotes

(a) $z = -0.05h$ (b) $z = -0.25h$
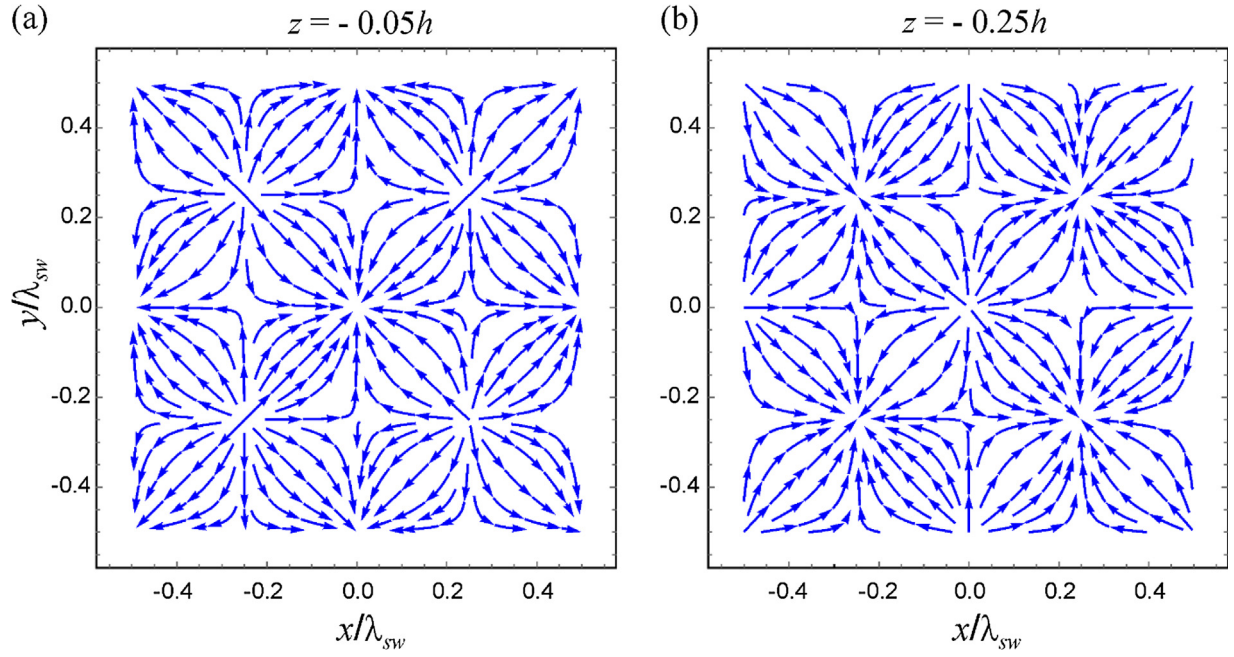
Fig. 5. Examples of calculation without the streaming cross terms. The parameters are as in Fig. 2a and b. The channel height h is 50 μm. Rotation is absent.

(a) $h = 30$ μm   (b) $h = 50$ μm

(c) $h = 80$ μm   (d) $h = 100$ μm
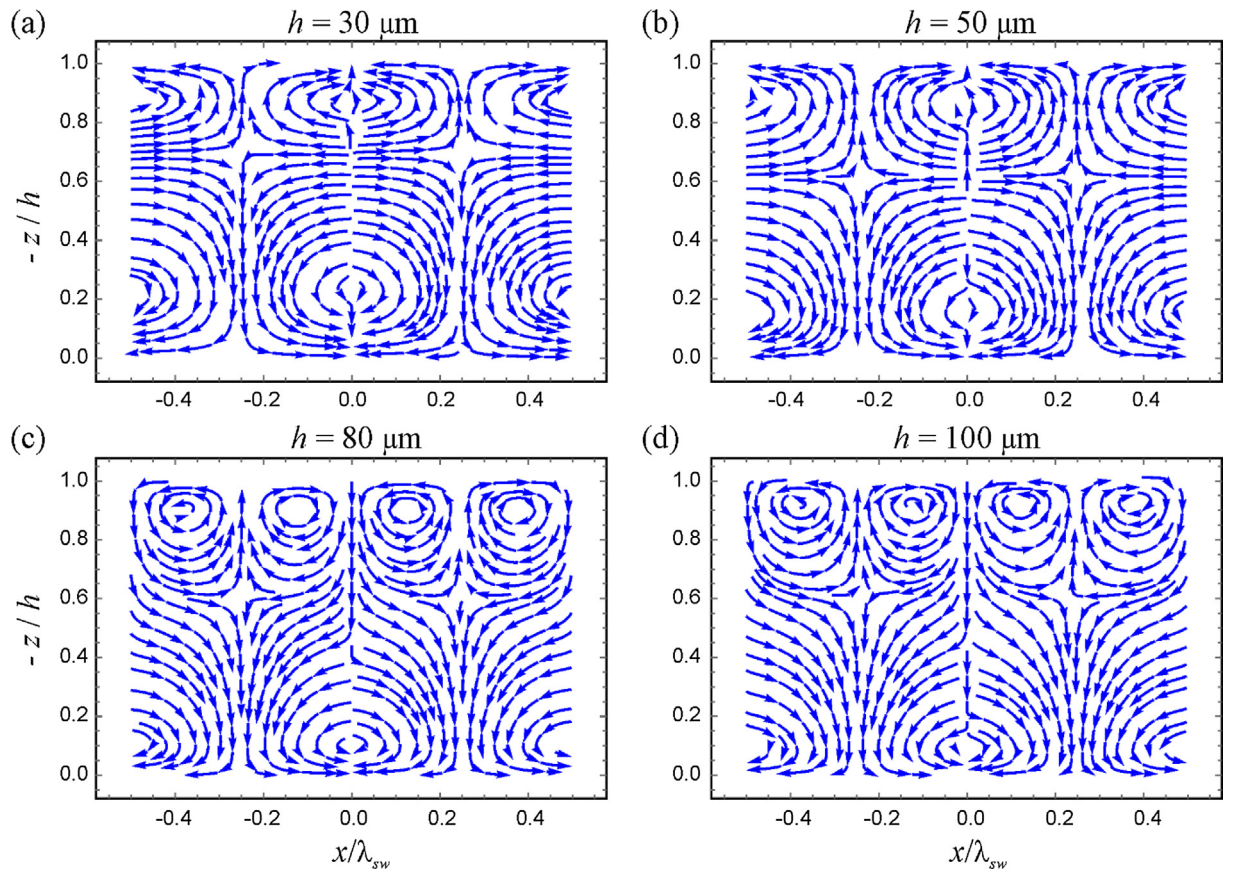
Fig. 6. Projections of streamlines of the Lagrangian streaming velocity on the xz plane at $y = \lambda_{sw}/4$ for different values of the channel height h. The phase lag between the x and y waves is $\phi = \pi/2$. Division into upper and lower parts is observed.
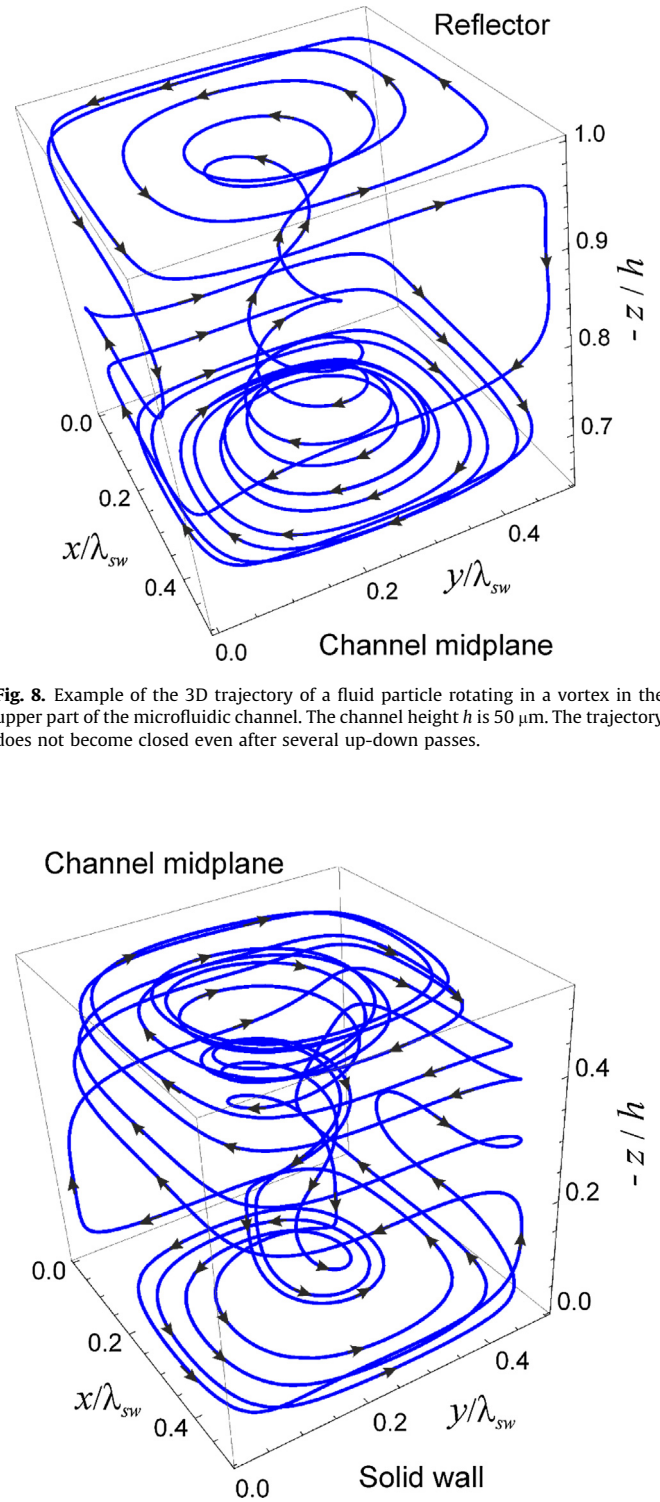
(a)

(b)
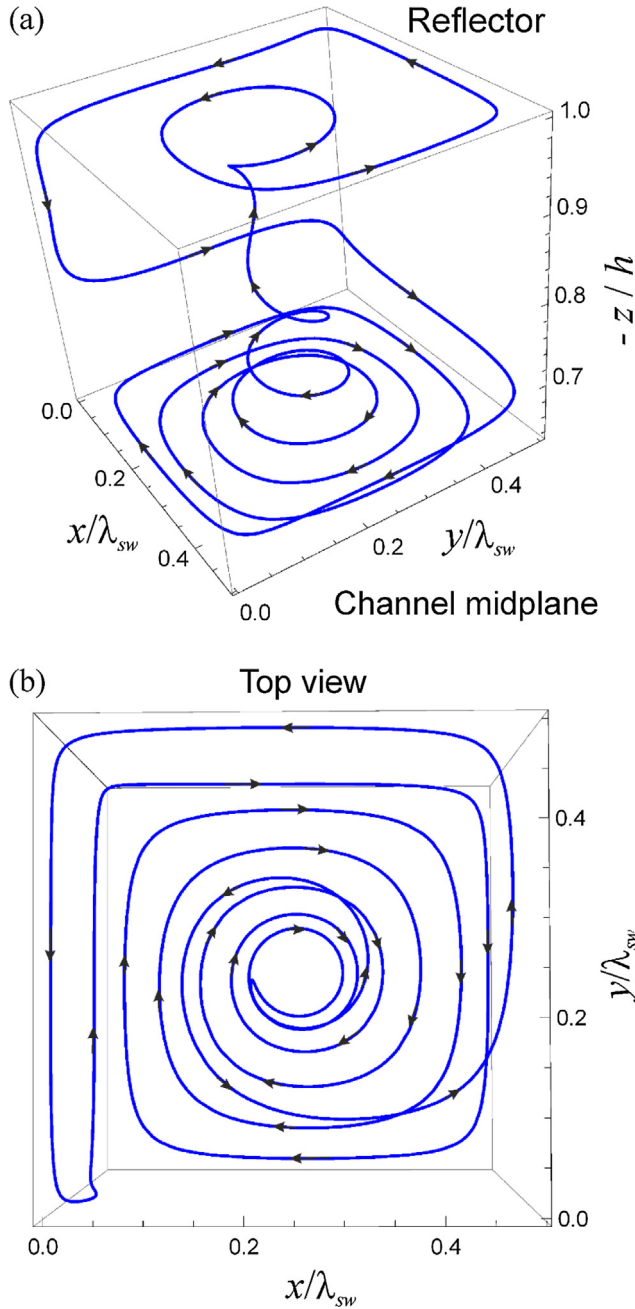
Fig. 7. Example of the 3D trajectory of a fluid particle rotating in a vortex in the upper part of the microfluidic channel. The channel height h is 50 μm. The trajectory becomes closed in one up-down pass.

Fig. 8. Example of the 3D trajectory of a fluid particle rotating in a vortex in the upper part of the microfluidic channel. The channel height h is 50 μm. The trajectory does not become closed even after several up-down passes.

Fig. 9. Example of the 3D trajectory of a fluid particle rotating in a vortex in the lower part of the microfluidic channel. The trajectory is not closed. The channel height h is 50 μm.

the ratio of the magnitude of the y wave to that of the x wave. Fig. 11 shows the transformation of the xz streamline pattern calculated at $y = \lambda_{sw}/4$, the parameters being the same as in Fig. 10. Fig. 11a corresponds to Fig. 6b. A moderate difference between the magnitudes of the waves does not give rise to noticeable changes in the xy streamline pattern; cf. Fig. 10a and b. However, changes in the xz streamline pattern are quite visible; cf. Fig. 11a and b. As one can see, the fluid rotation does not disappear even if the difference between the wave magnitudes is quite considerable. Fig. 12 shows how the 3D trajectory of a fluid particle depicted in Fig. 7 is transformed at $\varepsilon = 0.25$.

Fig. 13 gives an idea of the amplitude of the streaming velocity. Let us imagine that we cross the left top vortex in Fig. 2a, going

along the x direction through the vortex center. That is, $y/\lambda_{sw} = 0.25$, $-0.5 \leqslant x/\lambda_{sw} \leqslant 0$ and $z = -0.05h$. The solid curve in Fig. 13 shows how the amplitude of the Lagrangian streaming velocity varies in this case. The other curves show the same for the other values of z indicated in Fig. 2. The amplitude of the streaming velocity is proportional to the square of the amplitude
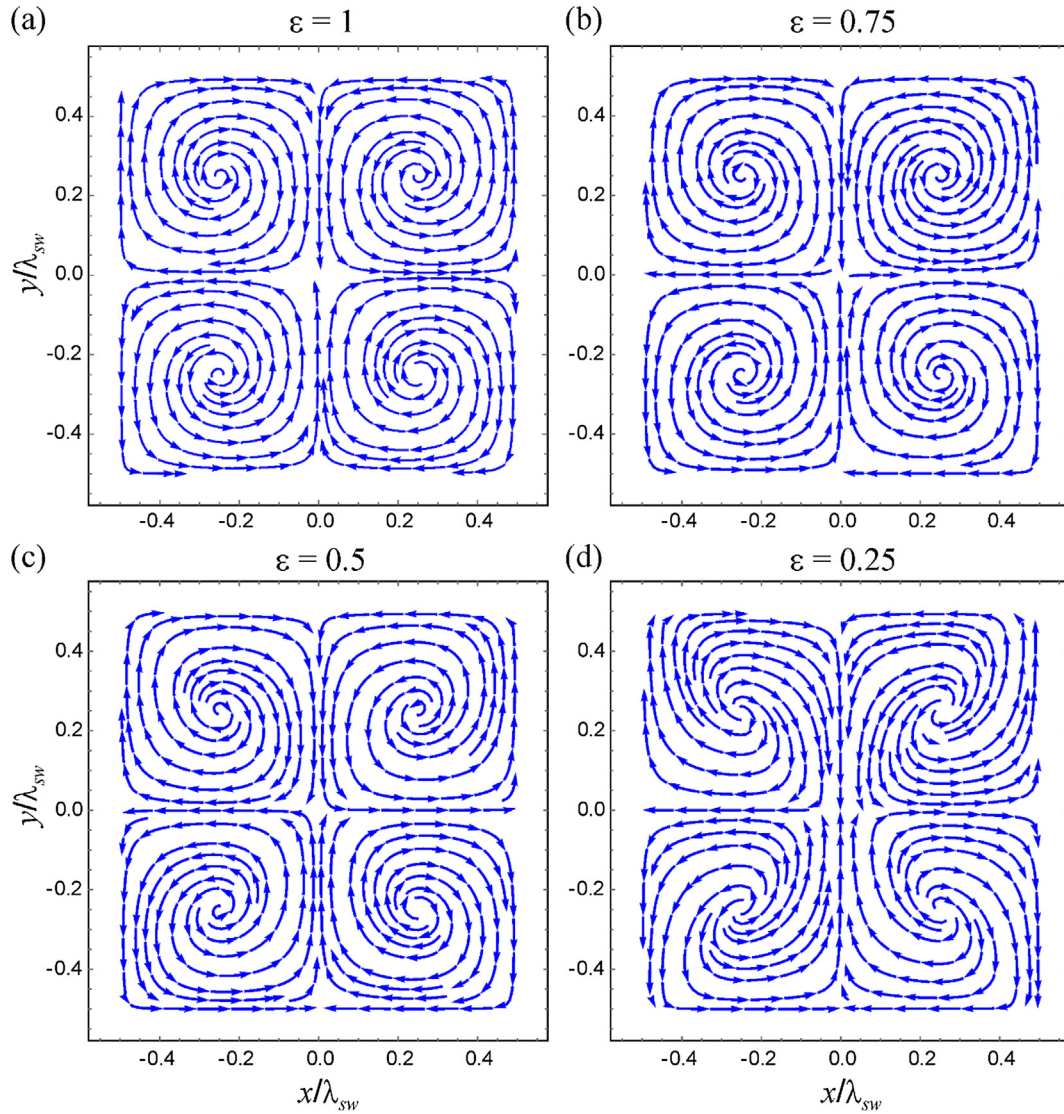
Fig. 10. Projections of streamlines of the Lagrangian streaming velocity on the xy plane at $z = -0.05h$ for different values of ε. ε is the ratio of the magnitude of the y wave to that of the x wave. $h = 50$ μm, $\phi = \pi/2$.

of excitation. In our case, excitation is the vibration of the solid wall, which is caused by counter-propagating leaky surface waves. It is shown in our previous paper [29] that the amplitudes of the surface waves can be specified in such a way that one can get a desired magnitude of the vertical displacement of the solid–fluid interface. Let us denote this quantity by Δz. It is pointed out in literature that it is difficult to measure experimentally the vibration of a solid substrate in a microfluidic setup [27]. Fig. 13 was calculated at $\Delta z = 0.1$ nm. We have chosen this value following Vanneste and Bühler [27] who used this value in their numerical simulations. As follows from what was said above, the values of the streaming velocity shown in Fig. 13 can be easily recalculated for any amplitude of excitation. The form of the curves will remain unchanged. As Fig. 13 shows, at $\Delta z = 0.1$ nm, the maximum amplitude of the streaming velocity is of the order of 0.5 μm/s.

4. Conclusions

A theory has been developed for the modelling of acoustic streaming in a microfluidic channel confined between an elastic

solid wall and a rigid reflector. The theory assumes that the acoustic streaming is generated by two orthogonal ultrasound standing waves of the same frequency that are created by two pairs of counter-propagating leaky surface waves induced in the solid wall. The magnitudes and phases of the standing waves are assumed to be, in general, different. Full analytical solutions were obtained for the equations of acoustic streaming in the situation under study. Particular numerical examples were considered to reveal the structure of the acoustic streaming. It has been shown that the interaction of the driving standing waves leads to the appearance of a cross term in the equations of acoustic streaming. If the phase lag between the standing waves is nonzero, the cross term gives rise to circular vortices with rotation axes perpendicular to the solid wall of the channel. The vortices make fluid particles rotate and move alternately up and down between the solid wall and the reflector.

The obtained results are of immediate interest for applications concerning the ultrasonic micromixing of fluids and the manipulation of microparticles in microfluidic devices. Furthermore, the possibility to induce a preferred direction in the fluid vorticity with
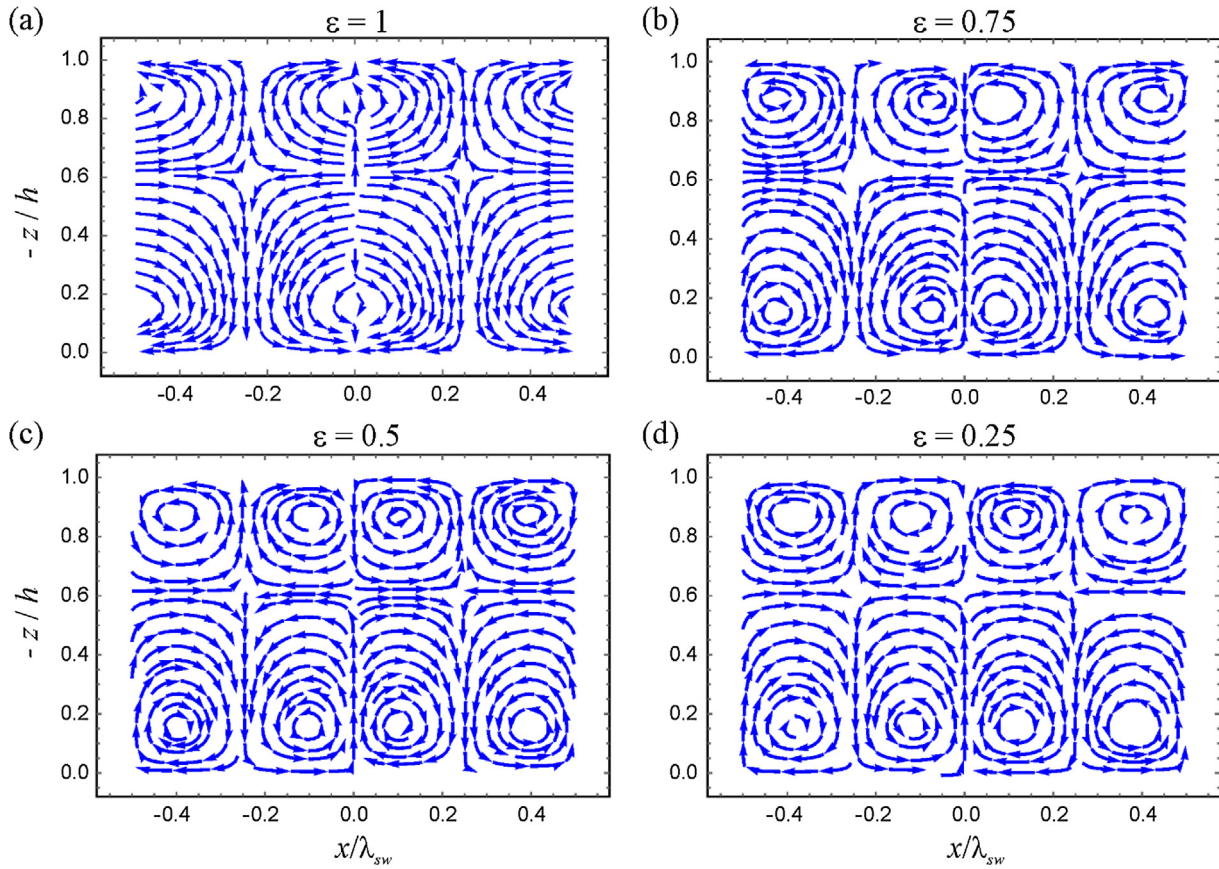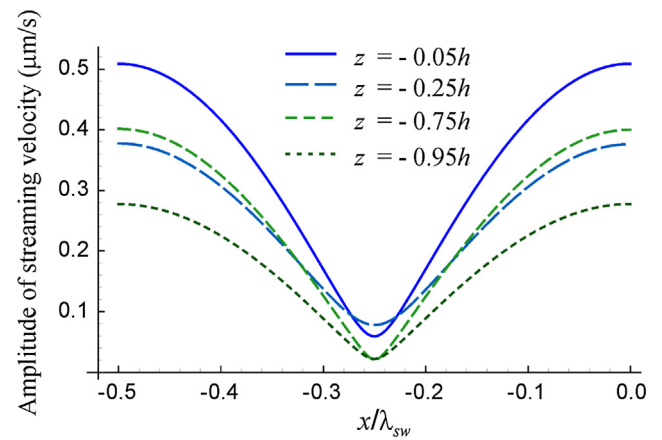
Fig. 11. Projections of streamlines of the Lagrangian streaming velocity on the xz plane at $y = \lambda_{sw}/4$ for different values of ε. ε is the ratio of the magnitude of the y wave to that of the x wave. $h = 50$ μm, $\phi = \pi/2$.
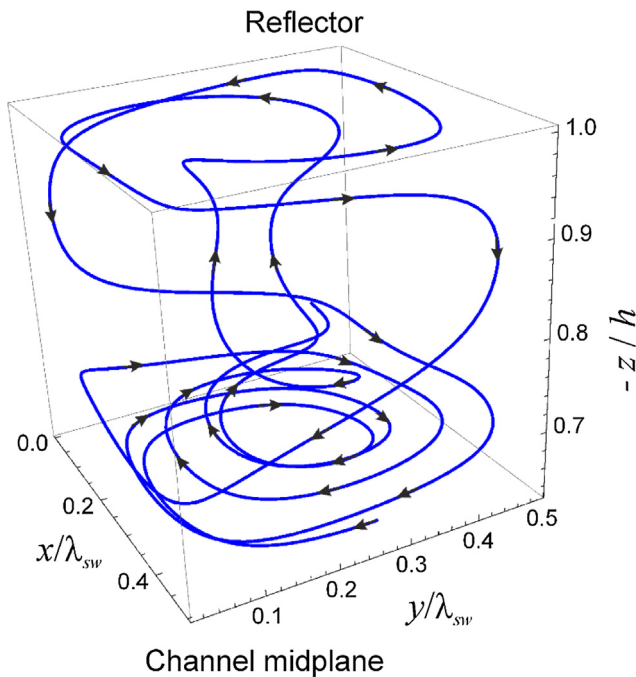
Fig. 12. Example of the 3D trajectory of a fluid particle at $\varepsilon = 0.25$. The other parameters are as in Fig. 7.

Fig. 13. Amplitude of the Lagrangian streaming velocity as a function of x at $y = \lambda_{sw}/4$ for different values of z. $h = 50$ μm, $\phi = \pi/2$. The amplitude of the vertical displacement of the solid-fluid interface Δz is 0.1 nm.

Appendix A. Derivatives of $s_{nx}s_{my}^*$

The superscripts II and IV denote the second and the forth derivatives with respect to z.

periodic alternate orientation can be of importance for exploiting properties of anisotropic fluids such as liquid crystals.

$$(s_{1x}s_{4y}^*)^{//} = (q_f^2 + q_v^{2*})s_{1x}s_{4y}^* + 2q_f q_v^* s_{3x}s_{2y}^*,$$

$$(s_{1x}s_{4y}^*)^{IV} = (q_f^4 + q_v^{4*} + 6q_f^2 q_v^{2*})s_{1x}s_{4y}^* + 4q_f q_v^*(q_f^2 + q_v^{2*})s_{3x}s_{2y}^*,$$

$$(s_{3x}s_{2y}^*)^{//} = (q_f^2 + q_v^{2*})s_{3x}s_{2y}^* + 2q_f q_v^* s_{1x}s_{4y}^*,$$

$$(s_{3x}s_{2y}^*)^{IV} = (q_f^4 + q_v^{4*} + 6q_f^2 q_v^{2*})s_{3x}s_{2y}^* + 4q_f q_v^*(q_f^2 + q_v^{2*})s_{1x}s_{4y}^*,$$

$$(s_{2x}s_{4y}^*)^{//} = (q_v^2 + q_v^{2*})s_{2x}s_{4y}^* + 2q_v q_v^* s_{4x}s_{2y}^*,$$

$$(s_{2x}s_{4y}^*)^{IV} = (q_v^4 + q_v^{4*} + 6q_v^2 q_v^{2*})s_{2x}s_{4y}^* + 4q_v q_v^*(q_v^2 + q_v^{2*})s_{4x}s_{2y}^*,$$

$$(s_{4x}s_{2y}^*)^{//} = (q_v^2 + q_v^{2*})s_{4x}s_{2y}^* + 2q_v q_v^* s_{2x}s_{4y}^*,$$

$$(s_{4x}s_{2y}^*)^{IV} = (q_v^4 + q_v^{4*} + 6q_v^2 q_v^{2*})s_{4x}s_{2y}^* + 4q_v q_v^*(q_v^2 + q_v^{2*})s_{2x}s_{4y}^*,$$

$$(s_{4x}s_{1y}^*)^{//} = (q_v^2 + q_f^{2*})s_{4x}s_{1y}^* + 2q_f^* q_v s_{2x}s_{3y}^*,$$

$$(s_{4x}s_{1y}^*)^{IV} = (q_v^4 + q_f^{4*} + 6q_f^{2*} q_v^2)s_{4x}s_{1y}^* + 4q_f^* q_v(q_v^2 + q_f^{2*})s_{2x}s_{3y}^*,$$

$$(s_{2x}s_{3y}^*)^{//} = (q_v^2 + q_f^{2*})s_{2x}s_{3y}^* + 2q_f^* q_v s_{4x}s_{1y}^*,$$

$$(s_{2x}s_{3y}^*)^{IV} = (q_v^4 + q_f^{4*} + 6q_f^{2*} q_v^2)s_{2x}s_{3y}^* + 4q_f^* q_v(q_v^2 + q_f^{2*})s_{4x}s_{1y}^*,$$

$$(s_{1x}s_{2y}^*)^{//} = (q_f^2 + q_v^{2*})s_{1x}s_{2y}^* + 2q_f q_v^* s_{3x}s_{4y}^*,$$

$$(s_{1x}s_{2y}^*)^{IV} = [(q_f^2 + q_v^{2*})^2 + 4q_f^2 q_v^{2*}]s_{1x}s_{2y}^* + 4q_f q_v^*(q_f^2 + q_v^{2*})s_{3x}s_{4y}^*,$$

$$(s_{3x}s_{4y}^*)^{//} = (q_f^2 + q_v^{2*})s_{3x}s_{4y}^* + 2q_f q_v^* s_{1x}s_{2y}^*,$$

$$(s_{3x}s_{4y}^*)^{IV} = [(q_f^2 + q_v^{2*})^2 + 4q_f^2 q_v^{2*}]s_{3x}s_{4y}^* + 4q_f q_v^*(q_f^2 + q_v^{2*})s_{1x}s_{2y}^*,$$

$$(s_{2x}s_{1y}^*)^{//} = (q_v^2 + q_f^{2*})s_{2x}s_{1y}^* + 2q_f^* q_v s_{4x}s_{3y}^*,$$

$$(s_{2x}s_{1y}^*)^{IV} = [(q_v^2 + q_f^{2*})^2 + 4q_f^{2*} q_v^2]s_{2x}s_{1y}^* + 4q_f^* q_v(q_v^2 + q_f^{2*})s_{4x}s_{3y}^*,$$

$$(s_{4x}s_{3y}^*)^{//} = (q_v^2 + q_f^{2*})s_{4x}s_{3y}^* + 2q_f^* q_v s_{2x}s_{1y}^*,$$

$$(s_{4x}s_{3y}^*)^{IV} = [(q_v^2 + q_f^{2*})^2 + 4q_f^{2*} q_v^2]s_{4x}s_{3y}^* + 4q_f^* q_v(q_v^2 + q_f^{2*})s_{2x}s_{1y}^*,$$

$$(s_{4x}s_{4y}^*)^{//} = (q_v^2 + q_v^{2*})s_{4x}s_{4y}^* + 2q_v q_v^* s_{2x}s_{2y}^*,$$

$$(s_{4x}s_{4y}^*)^{IV} = [(q_v^2 + q_v^{2*})^2 + 4q_v^2 q_v^{2*}]s_{4x}s_{4y}^* + 4q_v q_v^*(q_v^2 + q_v^{2*})s_{2x}s_{2y}^*,$$

Appendix B. Supplementary material

Supplementary data associated with this article can be found, in the online version, at https://doi.org/10.1016/j.ultras.2018.02.002.

References

[1] J. Dual, P. Hahn, I. Leibacher, D. Möller, T. Schwarz, J. Wang, Acoustofluidics 19: ultrasonic microrobotics in cavities: devices and numerical simulation, Lab Chip 12 (2012) 4010–4021.
[2] J. Friend, L. Yeo, Microscale acoustofluidics: microfluidics driven via acoustics and ultrasonics, Rev. Mod. Phys. 83 (2011) 647–704.
[3] B. Cetin, S. Buyukkocak, M.B. Özer, Microscale acoustofluidics, in: D. Li (Ed.), Encyclopedia of Microfluidics and Nanofluidics, Springer, New York, 2015, pp. 2149–2158.
[4] A. Lamprecht, S. Lakämper, T. Baasch, I.A.T. Schaap, J. Dual, Imaging the position-dependent 3D force on microbeads subjected to acoustic radiation forces and streaming, Lab Chip 16 (2016) 2682–2693.
[5] R.H. Liu, R. Lenigk, P. Grodzinski, Acoustic micromixer for enhancement of DNA biochip systems, J. Microlithogr. Microfabr. Microsyst. 2 (2003) 178–184.
[6] A.R. Tovar, A.P. Lee, Lateral cavity acoustic transducer, Lab Chip 9 (2009) 41–43.
[7] D. Ahmed, X.L. Mao, J.J. Shi, B.K. Juluri, T.J. Huang, A millisecond micromixer via single-bubble-based acoustic streaming, Lab Chip 9 (2009) 2738–2741.
[8] M. Wiklund, R. Green, M. Ohlin, Acoustofluidics 14: applications of acoustic streaming in microfluidic devices, Lab Chip 12 (2012) 2438–2451.
[9] Lord Rayleigh, On the circulation of air observed in Kundt's tubes, and on some allied acoustical problems, Philos. Trans. R. Soc. Lond. 175 (1884) 1–21.
[10] H. Schlichting, Berechnung ebener periodischer Grenzschichtströmungen, Calculation of plane periodic boundary layer streaming, Physikalische Zeitschrift 33 (1932) 327–335**.
[11] P.J. Westervelt, The theory of steady rotational flow generated by a sound field, J. Acoust. Soc. Am. 25 (1953) 60–67.
[12] W.L. Nyborg, Acoustic streaming near a boundary, J. Acoust. Soc. Am. 30 (1958) 329–339.
[13] W.L. Nyborg, Acoustic streaming, in: W.P. Mason (Ed.), Physical Acoustics, vol. 2B, Academic Press, New York, 1965, pp. 290–295 (Chapter 11).
[14] W.L. Nyborg, Acoustic streaming, in: M.F. Hamilton, D.T. Blackstock (Eds.), Nonlinear Acoustics, Academic Press, San Diego, 1998 (Chapter 7, Section 3.3).
[15] S. Boluriaan, P.J. Morris, Acoustic streaming: from Rayleigh to today, Int. J. Aeroacoust. 2 (2003) 255–292.
[16] M.F. Hamilton, Y.A. Ilinskii, E.A. Zabolotskaya, Acoustic streaming generated by standing waves in two-dimensional channels of arbitrary width, J. Acoust. Soc. Am. 113 (2003) 153–160.
[17] A.A. Doinikov, P. Thibault, P. Marmottant, Acoustic streaming generated by two orthogonal standing waves propagating between two rigid walls, J. Acoust. Soc. Am. 141 (2017) 1282–1289.
[18] P.B. Muller, R. Barnkob, M.J.H. Jensen, H. Bruus, A numerical study of microparticle acoustophoresis driven by acoustic radiation forces and streaming-induced drag forces, Lab Chip 12 (2012) 4617–4627.
[19] J. Lei, P. Glynne-Jones, M. Hill, Acoustic streaming in the transducer plane in ultrasonic particle manipulation devices, Lab Chip 13 (2013) 2133–2143.
[20] J. Lei, M. Hill, P. Glynne-Jones, Numerical simulation of 3D boundary-driven acoustic streaming in microfluidic devices, Lab Chip 14 (2014) 532–541.
[21] R. Barnkob, P. Augustsson, T. Laurell, H. Bruus, Acoustic radiation- and streaming-induced microparticle velocities determined by microparticle image velocimetry in an ultrasound symmetry plane, Phys. Rev. E 86 (2012) 056307.
[22] B. Hammarstrom, T. Laurell, J. Nilsson, Seed particle-enabled acoustic trapping of bacteria and nanoparticles in continuous flow systems, Lab Chip 12 (2012) 4296–4304.
[23] M. Gedge, M. Hill, Acoustofluidics 17: theory and applications of surface acoustic wave devices for particle manipulation, Lab Chip 12 (2012) 2998–3007.
[24] S.B.Q. Tran, P. Marmottant, P. Thibault, Fast acoustic tweezers for the two-dimensional manipulation of individual particles in microfluidic channels, Appl. Phys. Lett. 101 (2012) 114103.
[25] X. Ding, P. Li, S.-C.S. Lin, Z.S. Stratton, N. Nama, F. Guo, D. Slotcavage, X. Mao, J. Shi, F. Costanzo, T.J. Huang, Surface acoustic wave microfluidics, Lab Chip 13 (2013) 3626–3649.
[26] L.Y. Yeo, J.R. Friend, Surface acoustic wave microfluidics, Annu. Rev. Fluid Mech. 46 (2014) 379–406.
[27] J. Vanneste, O. Bühler, Streaming by leaky surface acoustic waves, Proc. R. Soc. A 467 (2011) 1779–1800.
[28] N. Nama, R. Barnkob, Z. Mao, C.J. Kähler, F. Costanzo, T.J. Huang, Numerical study of acoustophoretic motion of particles in a PDMS microchannel driven by surface acoustic waves, Lab Chip 15 (2015) 2700–2709.
[29] A.A. Doinikov, P. Thibault, P. Marmottant, Acoustic streaming in a microfluidic channel with a reflector: case of a standing wave generated by two counterpropagating leaky surface waves, Phys. Rev. E 96 (2017) 013101.
[30] I. Bernard, A.A. Doinikov, P. Marmottant, D. Rabaud, C. Poulain, P. Thibault, Controlled rotation and translation of spherical particles or living cells by Surface Acoustic Waves, Lab Chip 17 (2017) 2470–2480.
[31] C.E. Bradley, Acoustic streaming field structure: the influence of radiator, J. Acoust. Soc. Am. 100 (1996) 1399–1408.
[32] M.S. Longuet-Higgins, Viscous streaming from an oscillating spherical bubble, Proc. R. Soc. Lond. A 454 (1998) 725–742.
[33] C.P. Lee, T.G. Wang, Near-boundary streaming around a small sphere due to two orthogonal standing waves, J. Acoust. Soc. Am. 85 (1989) 1081–1088.
[34] A. Lamprecht, T. Schwarz, J. Wang, J. Dual, Viscous torque on spherical micro particles in two orthogonal acoustic standing wave fields, J. Acoust. Soc. Am. 138 (2015) 23–32.